DOI: https://doi.org/10.2138/am-2021-7578. http://www.minsocam.org/

Revision 2

X-ray computed microtomography of diamondiferous impact suevitic breccia and clast-poor melt rock from the Kara astrobleme (Pay-Khoy, Russia)

Aleksandr A. Zubov[1]*, Tatyana G. Shumilova[1], Andrey V. Zhuravlev[1], Sergey I. Isaenko[1]

[1] Institute of Geology of Komi Science Center of the Ural Branch of the Russian Academy of Sciences, Pervomayskaya st. 54, Syktyvkar, 167982, Russia

* Correspondence: dixares@gmail.com; Tel.: +78212240970

ABSTRACT

X-ray computed microtomography (CT) of impact rock varieties from the Kara astrobleme is used to test the method's ability to identify morphology and distribution of the rock components. Three types of suevitic breccias, clast-poor melt rock, and a melt clast from a suevite were studied with a spatial resolution of 24 μm to assess CT data values of 3D structure and components of the impactites. The purpose is first to reconstruct pore space, morphology and distribution of all distinguishable crystallized melt, clastic components and carbon products of impact metamorphism, including the impact glasses, after-coal diamonds, and other carbon phases. Second, the data is applied to analyse the morphology and distribution of aluminosilicate and sulfide components in the melt and suevitic breccias. The technical limitations of the CT measurements applied to the Kara impactites are discussed. Because of the similar chemical composition of the aluminosilicate matrix, glasses, and some lithic and crystal clasts, these components are hard to distinguish in tomograms. The carbonaceous matter has CT data value close to air, so the pores and carbonaceous inclusions appear similar. However, X-ray microtomography could be used to evidence the differences between the studied types of suevites from the Kara astrobleme using structural-textural features of the whole rock, porosity and the distributions of carbonates and sulfides.

Keywords: X-ray computed tomography, impactites, impact melt rocks, impact glasses, suevites, Kara astrobleme.

INTRODUCTION

Shock metamorphism in large impact structures is one of the important processes significantly affecting regional geology and mineral deposits formation. Approximately 190 impact craters on the Earth's surface are known (Schmieder and Kring, 2020; Earth Impact Database). Impactites are the products of meteorite impact events. Their general specifics and systematics have been described in numerous works (Stöffler and Grieve, 2007; Stöffler 2017; Osinski and Pierazzo 2013; French 1998; French and Koeberl, 2010; Masaitis et al. 1998 et al.). Impactites are divided into three groups: shocked rocks (non-brecciated, melt-free), impact melt rocks (clast-free, clast-poor and clast-rich), and impact breccias (lithic breccias and suevites; the latter contain lithic and melt clasts). The particulars of impactite formation are determined by numerous factors of the falling meteoritic bodies and by the compositions of target rocks. The Kara astrobleme is one of the largest astroblemes known on land, formed on a sedimentary target approximately 70 Ma ago (Machshak 1991; Masaitis et al. 1998; Koeberl et al. 1990; Trieloff et al. 1998; Masaitis 1999). The astrobleme is characterized by high concentrations of unusual after-coal diamonds and diamond pseudomorphs of organic relicts ("diamond fossils"; Shumilova et al. 2018; 2019b). One of the poorly studied aspects of this object is the diversity and structure of impactites, as well as the distribution and nature of diamond concentration levels. Among the impactites at the Kara astrobleme, clast-poor melt rocks form several layer-like bodies, some dykes and some vein glass bodies (Shumilova et al., 2020). The suevites are very widely distributed and have been divided into three types according to geological, morphological, and structural characteristics (Shumilova et al., 2019a). These types presumably formed from different target substrates: type I suevites – predominantly silicate substrate; type II – mainly carbonate substrate; and type III – mainly carbonaceous deposits (Shumilova et al. 2019). In addition, one of the most interesting varieties of the impactites in this astrobleme is that the impact melt rock has close spatial and genetic relationships with the type I suevites. In this regard, the assessment of the volumetric distribution of structural components in the varieties of clastic and melt impactites of the Kara astrobleme is very important. X-ray computed microtomography (CT) is one of the potentially promising methods for studying this type of shocked-generated complicated rock. In this study, the CT method was used to analyze the 3D structure of the impactites and attempt to estimate the distribution of impact diamonds within suevites, clast-poor melt rocks and melt clasts within suevites.

X-ray computed tomography is a non-destructive method for internal structure studies that was proposed by Godfrey Hounsfield and Allan Cormac (Hounsfield 1973). Over the past decades, this method has been proven in many branches of science, including geology (e.g. Wellington, Vinegar, 1987; Shtyrlyaeva et al. 2016). The method has been actively used in the study of planetary materials, meteorites, and space body testing products (e.g., Hanna & Ketcham 2017; Rubin et al. 2001; Russell and Howard 2013; Tsuchiyama et al. 2002; Uesugi et al. 2010, 2013). At the same time, the features of applying X-ray computed tomography to impactites, including breccia varieties, are not clear and remain relatively poorly considered in the literature. The exceptions are the studies by Koeberl et al. (2002) who described the internal structure of impactites from the craters of Bosumtwi (Ghana) and Ries (Germany), as well as the tektites of Muong Nong (Thailand). The purpose of the present work was to test the applicability of X-ray computed microtomography for the study of the 3D structure of suevite varieties, melt clast varieties in suevites, and clast-poor impact melt rocks of the Kara astrobleme. The three objectives were to: i) Assess attenuation coefficients (radiodensities) of the components of the suevites and melt rocks of the Kara astrobleme; ii) Reconstruct pore space, morphology and distribution of all distinguishable melt, clast components and carbon products of impact metamorphism, including the quantity and distribution of impact glasses, after-coal diamonds, and other carbon phases; and iii) Analyse the morphology and distribution of aluminosilicate and sulfide components of melt and clastic impactites.

MATERIAL

During field works in 2015 and 2017, we sampled melt rocks and suevites extensively on the territory of the giant diamondiferous Kara astrobleme (Pay-Khoy, Russia), from natural outcrops within the marginal part of the impact crater to the canyon of the middle course of the Anaroga River and outcrops on the Kara, Sopchayu, and Putyu Rivers. Five samples of the most representative varieties of impactites, namely three types of suevites (Shumilova et al. 2019a), impact melt rocks, and a clastic melt fragment from the type II suevites were selected for our microtomographic study (Table 1).

The studied samples have been described earlier (Shumilova et al. 2019a; Shumilova et al. 2018; Golubev et al. 2018), and their characteristics are summarized in Table 1. The suevite I samples consist of melt-bearing breccia, containing more than 10–60 volume % of bombs and debris of impact glass (vitroclasts). The other components are fragments of rocks (lithoclasts) and minerals (crystal-clasts) from the target in different proportions, as well as fine-grained matrix, dispersed among the clasts (Masaitis 1998). The suevite II samples, in contrast to the suevite I, are characterized by higher content of limestone debris and predominantly carbonate cement; the suevite III samples are enriched in carbonaceous matter. These rocks differ significantly from one another in their geomorphological features in outcrops, structural-textural and material characteristics, colour and porosity as identified in the field conditions in 2015 (Shumilova et al. 2019a). The impact melt rock is either a massive or pore impactite, quenched from silicate impact melt and consisting of a glassy, hemi- or holocrystalline matrix, usually comprising 10–15 %

DOI: https://doi.org/10.2138/am-2021-7578. http://www.minsocam.org/

(rarer up to 30 %) of fragments of rocks and minerals that show signs of impact metamorphism and interaction with the melt (Masaitis 1998). The degree of impact melt crystallization was determined by X-ray diffraction (Isaenko et al. 2018).

The suevite varieties of the Kara astrobleme have similar chemical composition (Shumilova et al., 2019a) but differ significantly in terms of lithology of lithoclasts (Maksimenko et al. 2018). The lithoclasts in the suevites are characterized by sandstones, siltstones, shales, carbonate rocks, and products of various degrees of their mechanical and thermal alteration, including vitroclasts (Isaenko et al. 2018; Maksimenko et al. 2018).

METHODS AND EQUIPMENT

The samples were cut to cylindrical shape with sizes of approximately 4 cm diameter by 4 cm height. Mineral samples (graphite, quartz, and calcite) were used as radiodensity “standards” for comparison to the impactite components. The samples were oriented so that the axis of the cylinder was perpendicular to the X-ray beam. Tomographic studies were performed using a SkyScan 1173 (Bruker) microtomograph with a Hamamatsu 130/300 microfocus X-ray source, and analytical work was performed at St. Petersburg Mining University (St. Petersburg, Russia). Samples were studied with a lead-containing glass filter at an accelerating voltage of 120 kV and a source current of 66 μA according to the procedure developed earlier (Shtyrlyaeva and Zhuravlev, 2016). The mean energy of the X-ray radiation after filtering was about 90 KeV. The exposure time per projection was 1.05 seconds, 1200 projections were made on the rock sample.

After X-ray computed microtomography (CT) data collection, the examined samples were cut in half for visual examination and comparison of the tomographic sections with the corresponding surfaces of mechanical sections by optical microscopy, as well as for diagnosis of individual components by Raman spectroscopy. Smaller fragments of the samples were examined by scanning electron microscopy and microprobe analysis with a VEGA 3 TESCAN scanning electron microscope (Tescan, Czech Republic) accompanied by a VEGA 3LMN, INCA ENERGY 450 energy dispersive detector for chemical composition control and morphological details (at the Institute of Geology of Komi SC UB RAS, Syktyvkar, Russia). Optical observations were made with a POLAM P-312 (LOMO) combined polarization microscope, and Raman spectra were obtained by a Raman spectrometer (LabRamHR-800, Horiba Yuvon Jobin) at the Geoscience Center for Collective Use at the Institute of Geology of FRS Komi SC UB RAS (Syktyvkar). Spectra registration parameters were as follows: He-Ne laser (λ = 632.8 nm), power 2 mWt, a spectrometer grade 600, confocal hole size – 300 μm, spectral hole - 100 μm, objective magnification × 50, accumulation time for a signal – 3 seconds, 5 counts for a spectrum section. The spectra were recorded at room temperature with 1 μm spatial and 1 cm^{-1} spectral resolutions.

Computed tomography data sets were reconstructed using a NRecon (Bruker) software with correction for beam hardening and removing ring artefacts (software configuration applied: beam hardening correction = 41 %, ring artefact correction = 20). The voxel size of the tomograms is 25 μm. The computed tomography data values (CT data values) were used for subsequent data analyses. The CT data values are considered as an apparent proxy for the true mineral attenuation coefficient. CT data were visualized and analyzed with specialized software (DataViewer and CTvox, Bruker).

First, we chose a relatively low resolution of the tomograms (μm) to analyze rather large samples, which technically cannot be studied using nano-tomography. Second, the use of nanometer resolution for the tomograms of these samples significantly reduced their field of view. This action, given the very complex structural-textural and compositional specialization of the impactites, resulted in the loss of representativeness of a single sample, which was technically difficult and very time-consuming and did not present a reliable representation of the studied objects.

For comparison, porosity was determined by the difference in the weights of dry and water-saturated samples, multiplied by the density of the water. The water was infiltrated in the sample at atmospheric pressure through draining from open pores. The required value of porosity is calculated by the ratio of pores volume to the sample's volume (I.A. Preobrazhensky`s method (Ivanov et al. 2008)).

The protocol of the performed studies was generally as follows:

1 - On the basis of the reference section (in this case, the central section of the tomogram), CT data values profiling of the tomogram was performed for the most typical objects that had high constrast;

2 - Objects on the tomogram were classified by building a multimodal histogram according to the profiling data obtained at the previous stage;

3 - Pore space was reconstructed by global threshold binarization (segmentation) with a CT data values ranging from 0 to X for each section of the tomogram, where X is the maximum CT data value for the pore space, determined by the results of profiling (it varies insignificantly between the studied impactites);

4 - The morphology of the clast components of suevite was reconstructed by applying a median filter with a radius of 20 pixels (500 μm) to each section for noise reduction, followed by applying a modified (multilevel) algorithm (Ping-Sung Liao et al. 2001) of the Nobuyuki Otsu threshold binarization (Otsu 1979) based on the Yasunari Tosa open source software. The choice of the radius of the median filtering applies to the maximum size of inhomogeneity of the reconstructed suevite fragments;

5 - The morphology of the sulfide component was reconstructed using a global threshold binarization with a CT data value range determined from the results of the profiling. All binarization and reconstruction operations were performed at 8-bit CT data values.

RESULTS

X-ray tomography artefacts in impactites

During imaging and subsequent computer processing of shadow projections, a number of effects arise, both physical and computational, resulting in various artefacts on the tomograms (Hanna et al. 2017; De Man et al. 1999; Hsieh 2009; Ketcham 2006; Krumm 2006). A significant portion of these effects is compensated by computational algorithms and imaging techniques, including filters and imaging conditions. Unfortunately, complete compensation was not achieved; therefore, two types of artefacts were observed on the examined tomograms of the suevites, which extent affect the results of the subsequent processing.

Figure 1a, b shows artefacts expressed by an apparent increase in the CT data value on the interface of contrasting media. The artefact is caused by poly-chromaticity of the X-ray radiation used. The effect can be reduced by choosing the analyzed volume inside the sample.

Because the standards were set on top of the samples, artefacts of several types appeared on the tomograms of the samples. In Figure 2, the area labelled S2 has an artifact resulting from significantly different attenuation coefficients of the media (aluminosilicate solid body and air); that of S3 was due to an effect similar to the previous one; and that of S4 was caused by a cylindrical plume of apparent decrease in the attenuation coefficient propagating from the standard which has a high attenuation coefficient (in this case, calcite) towards the center of the sample, and enhanced by the features of the reconstruction algorithm.

Mineral reference specimens

Three homogenous mineral specimens (graphite, quartz, and calcite) were scanned together with the samples of the suevites. These specimens were used as reference materials (standards) for CT data value calibration of the images. On a multimodal histogram demonstrating the distribution of the attenuation coefficients (Fig. 3), these mineral standards are clearly divided into three classes by the CT data value intervals as follows: graphite – from 0.017 to 0.028, quartz – from 0.082 to 0.102, and calcite – from 0.136 to 0.184 1/mm. Since these ranges do not overlap, these minerals can be easily distinguished on a tomogram. This means that if a sample is represented by only these minerals, they should be distinguishable on the tomograms under specified conditions of acquisition of computed tomography data.

However, natural objects are much more complicated in their structural and chemical structure than the standards. At this stage, it became clear that the task of determining the spatial distribution of carbonaceous matter in the suevites and melt-bearing impactites could not be accomplished under the given imaging conditions because the distribution of the CT data values of graphite essentially overlap with that of the CT data values of pore space (Fig. 3). Therefore, the carbon particles in this case cannot be identified due to the substantial porosity of the studied impactites.

Determining the distribution of the components on X-ray tomograms depends mainly on the attenuation coefficients of the materials (Fig. 4). According to the data from silicate rock analysis and energy dispersive spectral analysis, the suevites and melt rocks of the Kara astrobleme are mainly represented by an aluminosilicate component with admixtures of silicate, carbonate, and sulfide components (Shumilova et al., 2018b). To supplement the specifics of previously identified varieties of suevites, we determined the nature of the distribution of each of these components, which primarily depended on the phase contrast on the tomograms.

Suevites

The suevites are chemically represented by aluminosilicates and silicates containing carbonate and carbonaceous inclusions. The suevite sample Kr-135 (type III suevite) represents impact breccia. The CT data values were profiled for the suevite matrix, debris in suevites, melt rock matrix, and pore space (Fig. 6a). Based on these profiling data, we designed a series of multimodal histograms for several matrix measurements (Fig. 6b) as well as for the clast component (Fig. 6c). On the histogram of the matrix measurements, the modes are seen to have almost the same parameters, with the exception of a small deviation apparently caused by the profile crossing strongly porous altered aluminosilicate melt fragment (L1 on Fig. 6).

The histogram of the clast components has significant interclass overlap, which is caused by the similarity in the chemical compositions of mineral components composing lithologically different debris of the target rocks. At this stage, this interclass overlap makes distinguishing the clastic components impossible because the clast components of the suevites are heterogeneous. This is shown in Figure 6d, a histogram showing a significant interclass overlap of the attenuation coefficients for the matrix, clast components, and pores. This feature greatly complicates the reconstruction of the morphology of the clast components, which casts doubt on their separation by the usual sampling from the voxel matrix of the tomogram.

Distribution of the pores and aluminosilicate, carbonate, and sulfide components were reconstructed by a global sampling of the voxel matrix of tomograms based on local CT data values using measurements of the mineral “standards”. As a result, the visualization of component data in space at a qualitative level was obtained (Fig. 7).

Reconstruction of the pore space and carbonaceous material is a non-trivial task since artefacts appear during imaging (Fig. 1), which prevents further work with the porosity model (Shtyrlyaeva et al., 2016). Pore space and carbon matter appearing similarly in the tomograms, it is impossible to distinguish the carbon material, compounded by its small particle sizes. This includes microdiamonds with overage size about 30-50 μm, i.e. very close to the resolution size of the used CT. However, for the purpose of identifying pore space, applying the criterion for selecting values of the CT data in the range from 0.01 to 0.02 1/cm is sufficient according to the profiling data. We designed the reconstruction of the pore space in samples of three types of suevites (Fig. 7). In the Kr-232 sample (type I suevite), the pore space is distributed almost

DOI: https://doi.org/10.2138/am-2021-7578. http://www.minsocam.org/

uniformly, with the tomogram displaying areas of severe fracturing. Additionally, this type is characterized by the presence of flow patterns that are visually distinguishable but do not appear on the tomograms. In sample Kr-61 (type II), the porosity is non-uniformly distributed and absent in fragments with carbonate. Suevite Kr-135 (type III) is characterized by the highest porosity.

The carbonate component of the suevites of the Kara astrobleme differs significantly from the aluminosilicate component. The former is localized mainly within the clastic part. The diffused form of carbonate is also irregularly distributed over the entire volume of the matrix of suevite and melt rock. It is notable that an apparent decrease in attenuation coefficients ("shadow" artefact, Fig. 2) occurs at the border of the sulfide component and the matrix of the suevite. The "shadows" indicate CT data values close to those of carbonates. Consequently, this effect led to adding a false additional volume to the reconstruction of the carbonate component.

The application to the tomogram sections of a median filter with multilevel segmentation using Otsu's criterion allows to partially minimize the problem of heterogeneity of the clast component in the CT data values. However, some fragments with CT data values close to those of the matrix, especially those with sizes of less than the window of the median filter, are lost during the reconstruction. Therefore, the determination of the morphometric characteristics of the clast component of the suevites is not carried out in this paper.

Clast-poor melt rock

The clast-poor melt rock (sample Kr-72) is characterized by an homogenous chemical composition with some local differentiation of impact melt. The X-ray tomogram of a melt rock sample emphasizes the nature of its melt formation (Fig. 8a). Small areas of increased CT data value are likely related to partially melted zones of target rock fragments. The pore space in the melt rock (Fig. 8b) is characterized by an irregular distribution, with the formation of empty "clusters" up to 5 mm in size.

This is the peer-reviewed, final accepted version for American Mineralogist, published by the Mineralogical Society of America.
The published version is subject to change. Cite as Authors (Year) Title. American Mineralogist, in press.
DOI: https://doi.org/10.2138/am-2021-7578. http://www.minsocam.org/

Melt fragment from suevite

Apart from lithic clasts, melt fragments are common in suevite. The studied melt clast (sample Kr-41) of aluminosilicate composition in suevite is a fragment of target rock after significant thermal overprint with almost complete melting. On the tomogram (Fig. 9) of the melt fragment, flow texture is evidenced by the distribution of two contrasting phases – aluminosilicate and pore space (Fig. 9b). Note that by the obtained attenuation CT map well corresponds to the natural color map in the sample. A study of the two phases by Raman spectrometry shows that one phase is of anatase-orthoclase (Fig. 10a) composition while the other is carbon (Fig. 10). Two lines are clearly distinguished in the Raman spectra: 143 cm^{-1} (anatase, Fig, 10d)) and 515 cm^{-1} (orthoclase, Fig. 10c). In the main orthoclase phase of the crystallized impact melt, the optically distinguishable particles of the carbon substance are uniformly distributed. This carbon substance has a similar Raman spectra to the standard of glass-like carbon (Fig. 10f) with a D band at 1330 cm^{-1} with the full width at half maximum (FWHM)=95 cm^{-1}, a G band at 1601 cm^{-1} with FWHM=60 cm^{-1} and second-order bands at 2643, 2912, and 3184 cm^{-1}. The sizes of carbon particles are 2–7 µm, i.e. several times smaller than the used resolution of the X-ray tomography (24 µm).

Figure 11 shows element maps of melt clast Kr-41, indicating a uniform distribution of the elements and the presence of many pores filled by thin crusts of SiO_2 and smectite. This image shows a large number of pores of different size, including small pores of a few µm. In addition, the image shows regions containing various content of carbon matter (CR and CP fields).

Carbonaceous substance. Due to the low X-ray attenuation of carbon substances, close to those of pores (i.e., to air), to their small particle sizes (approximately 50 µm or less), and to the relatively high contrast of the enclosing matrix with a relatively high density, visualizing the carbonaceous substance in the impactite by X-ray tomography would seem impossible.

However, if the X-ray tomography data is accompanied by the additional information, the partial analysis of the distribution of carbon particles in the studied melt fragment from suevite II (sample Kr-41) is possible. According to optical observations and Raman spectroscopic data, the aluminosilicate matrix in the optically grey areas of the sample contains uniformly scattered carbon particles, which spectroscopically correspond to glass-like carbon (Fig. 10c) (Ferrari and Robertson 2004; Isaenko et al. 2018a, 2018b). Moreover, the grey areas with carbon exhibit significantly reduced CT data values compared with the light zones of anatase-orthoclase composition (Fig. 9b). Therefore, the uniformly distributed particles of carbonaceous substance (glass-like carbon) 2–7 μm in size, accounting for approximately a few percent in concentration, and using an X-ray tomography resolution of 24 μm, allows to reduce the resulting CT data value of the aluminosilicate matrix. In conclusion, X-ray tomography (Fig. 9) combined with Raman spectroscopy (Fig. 10) and optical observations allows the determination of the distribution of glass-like carbon, a product of the impact transformation of a carbonaceous substance in a crystallized impact melt. We have determined that fine carbonaceous particles are scattered rather regularly in the grey zones of the melt fragment and arranged according to the texture of the solidified melt flow.

Pore space. Generally, the reconstructed pore space of the studied impactites differs in the varieties of suevites and melt rock in quantity, size, and degree of porosity. Quantitative data obtained on the porosity of the three types of suevites according to tomography and to I.A. Preobrazhensky`s method (Ivanov et al. 2008) are very different; e.g., they differ by 3.5 times for suevite type III (Table 2, sample Kr-41). On the other hand, the data on spatial reconstruction of the pore space and/or carbon substance (Fig. 7 d-f) fairly well reflect the distribution of voids in different suevites according to their genetic specificity.

Suevite type I is characterized by a "vein-like" distribution of the thinnest pores. In suevite II, the pores are usually quite large and confined to the boundaries of clasts. Suevite type III has the highest porosity with different sizes of voids that occur in the matrix and inside the fragments (Fig. 11). However, due to the overlapping of the fields of CT data values of carbon particles and void space, separating these phases on tomograms is impossible, and all we see is a reconstructed summed image.

During X-ray tomography of the suevites from the Kara astrobleme, we encountered problems at the segmentation stage caused by the following factors: homogeneity of the chemical composition of the studied samples; low spatial resolution of tomograms relative to the studied objects; and the presence of artefacts on the tomograms.

DISCUSSION

The method of X-ray computed microtomography allows to obtain reliable information on the structural and textural characteristics and material compositions of the three types of impactites in the Kara astrobleme and is promising for studying the different phases and rock structural features of other impactites.

The data obtained from the X-ray computed microtomography of suevite varieties (Figs. 7) clearly indicate that the originally proposed genetic specificity of the studied varieties in the Kara astrobleme is reflected on the tomograms by the degree of contrast and the nature of the clast component and the matrix. At the same time, the contrast in CT data values of melt rock appear only between the aluminosilicate matrix and the pore spaces and/or carbon substances, sulfides, and iron oxides. The structure of the matrix of the melt rock has a low contrast, which is caused by weak differentiation of the impact melt; consequently, the composition is homogeneous. This

This is the peer-reviewed, final accepted version for American Mineralogist, published by the Mineralogical Society of America.
The published version is subject to change. Cite as Authors (Year) Title. American Mineralogist, in press.
DOI: https://doi.org/10.2138/am-2021-7578. http://www.minsocam.org/

microcrystalline structure is the result of rapid crystallization, resulting in the silicate mineral phases having sizes below the spatial resolution of the tomograms. Additionally, completely melted relicts of target rocks show weak contrast and their outlines are optically poorly visible and are almost completely lost in X-ray images (Fig. 8). Crystallized impact melts and amorphous glasses, with almost the same elemental composition and cryptocrystalline structure (Fig. 11), are also indistinguishable on the tomograms.

The schlieren texture, which results from the differentiation and solidification of the impact melt during its movement, characterizes the melt clastogenic fragment from suevite I. The presence of micro-sized particles of glass-like carbon (2-7 μm – less than the tomogram resolution) in the matrix complicates the process of reconstructing mineral phases since the small particle size and low spatial resolution of the tomograms cause underestimation of the attenuation of the anorthite-orthoclase matrix containing these particles. However, this effect can be qualitatively used to determine the concentration of carbon particles in samples of similar type. Additionally, it is notable that the pore space in the melt clastogenic fragment (Fig. 9c) does not follow the flow pattern (Fig. 9a), which might indicate that pores formed in the melt when it was solidifying during stagnation.

The porosity is reconstructed quite well in tomograms; however, its quantitative determination for the studied impactites is distorted. The quantitative characteristics of porosity of the three types of suevites vary greatly, as determined by tomogram reconstruction using X-ray tomography data and I.A. Preobrazhensky's method (Table 2). This could be caused by the numerous pores in the suevites having a smaller size (Fig. 11) than the spatial resolution of the tomograms (24 μm).

As a first result of our study of a clastogenic melt fragment and clast-poor impact melt rock from the Kara astrobleme, we clarify the following features regarding application of the X-ray computed microtomography.

On the tomograms of the studied suevites, we observe a weak contrast in the CT data values of the aluminosilicate matrix of the suevite type I to the litho- and crystal-clasts, which is related to their similar chemical compositions. In the suevites types II and III, the contrast on the tomograms is more pronounced due to the significantly more diverse composition of the components.

The X-ray computed microtomography of the melt rock from the Kara astrobleme is characterized by low X-ray contrast in the CT data due to the compositional homogeneity of the melt, a consequence of the similar chemical composition of the target lithological components.

Analysis of the phase contrast of the impactite components on the tomograms shows that the impact glasses (fine-grained particles) in the suevite matrix do not differ due to their low CT data value contrast in respect to aluminosilicates and silicates of the enclosing material. The carbonate component is quite well recognized, depending on the type of impactite, and it has a different content and distribution compared to the silicates. Sulfides are also clearly distinguished. The reconstructed characteristics of porosity in both the clast-poor impact melt rock and clastogenic impact melt fragment can be observed by this method, but under the used conditions for the X-ray tomograms record, these features are greatly weakened due to the relatively low spatial resolution of the tomograms and the presence of porosity smaller than the threshold resolution of the applied microtomography in the melt elements.

As a second result of our study, the X-ray tomographic method allows clarification of the difference between the studied types of suevites from the Kara astrobleme by 3D structural rock features, porosity and the distributions of carbonate and sulfides.

It is widely known that impactites can be affected by post-impact hydrothermal alteration (Naumov, 2002, 2005; Osinski et al, 2013; Kring et al., 2020; Pirajno, 2005 and others). The X-ray tomograms could be expected to provide 3D spatial information on the alteration character. According to Naumov (2005), two different types of post-impact hydrothermal alteration can occur in peripheral impactites – autometasomatism and circulating solutions with hydrothermal mineralization. The latter is characterized by vein bodies with pyrite, calcite, and analcime (Naumov, 2002).

In the peripheral Kara impactites studied here, located in the southern part of the astrobleme, hydrothermal alteration is present as little altered suevites and melt bodies, with probable autometasomatic alteration by calcite and pyrite redeposition within the water-rich and porous suevites. The post-impact hydrothermal veins are rare within the suevites and have thicknesses of 30-50 cm. Here, we did not studied the vein hydrothermal mineralization, but targeted all the structural-textural composition of the Kara impactites prior to hydrothermal alteration.

Within the impact melt occurrences at the studied region of the Kara astrobleme, hydrothermal alteration generated smectite within their pore space, as observed by SEM (Shumilova et al, 2020). This smectite may not be related to autometasomatic alteration, but to general melt rock solidification with minerals formation during impact melt cooling – crystallization (Osinski et al., 2013). Shumilova et al. (2020) proposed that the smectite that has been found within the ultrahigh-pressure high temperature impact melt vein glasses containing melt-crystallized single-crystalline coesite (Shumilova et al, 2020). Origin of the smectite is beyond the scope of this paper. Finally, our X-ray tomography data did not evidence any hydrothermal alteration by any specific minerals distribution, probably due to autometasomatic character of carbonate redeposition within the studied suevites and the level of the X-ray microtomography resolution. The clay alteration was not distinguished in this work due to low clay content and low X-ray contrast within the original host mineralization.

In summary, the provided CT data demonstrate that CT microtomography can be used for the 3D-petrology study of impactites for their general structural and textural characteristics and for their breccia clasts characteristics. The technical limitations as applied to the Kara breccia and melt impactites are explained by lithic components having low compositional contrast for X-ray mapping and sizes below the microtomography resolution limits.

IMPLICATIONS

The obtained data demonstrate that the method of X-ray computed microtomography has some limitations for the study of the Kara impactites. These are due to the weakly contrasting X-ray absorption of the impactites mineral components with similar chemical composition and to the resolution of microtomography applied to slightly differentiated cryptocrystalline systems formed as a result of rapid crystallization from an impact melt. Considering the specific nature of the target rocks of the Kara astrobleme, characterized by complex alternations of sedimentary rocks with different lithology but similar chemical compositions and a significant proportion of black shales and limestones, interpreting the X-ray microtomography results is complex and requires higher resolution without reducing of the analysis volume. The presented results point to the need to use CT micro- and nanotomography in combination. Microtomography of the Kara impactites would provide the general 3D petrological information of the whole rock while nanotomography would shed light on tiny details, including microdiamonds if present within within the small volume analyzed, given that their concentration is low in these rocks. On the other hand, chemically heterogeneous impactites having larger differences in the composition of their components compared to the Kara impactites can be effectively studied by X-ray microtomography.

The effect of “underestimation” or “overestimation” of the natural attenuation coefficients of the materials that we evidenced is due to the high contents of fine dispersed and strongly contrasting micro-size phases. This indicates a possible application of such indirect information to obtaining 3D-information about the distribution of micro-size phases within the host rock.

Another application is to evidence different kinds of materials with contrasting inclusions and structural defects.

Finally, the presented methodology, the determined artefacts from this survey and the interpretation of the data from X-ray computed tomography of the impactites from the Kara astrobleme can be applied to impactites from other astroblemes, and any other poly-mineral systems and materials.

ACKNOWLEDGEMENTS

The authors are grateful to A.A. Shtyrlyaeva and E.M. Tropnikov for their assistance with the analytical work. The study was carried out under the framework of the RSF project # 17-17-01080 for the analysis of melt components of the Kara impactites; analytical measurements were provided with instrumental equipment of the Center of Collective Use of the Saint Petersburg Mining University (Saint Petersburg, Russia) and the Center of Collective Use “GEONAUKA” (Syktyvkar, Russia) funded through NIR GR #AAAA-A17-117121270036-7.

AUTHOR CONTRIBUTIONS

A.A.Z. – geological field study, optical microcopy, CT data interpretation, paper writing; T.G. Sh. – initial idea, organizing and heading of geological field studies, sampling, specimens preparing, participation at all stages of analytical works, paper editing; A.V.Zh. – CT data interpretation, participating in paper writing; S.I.I. – participation at field works, detail Raman spectroscopy studies.

CONFLICTS OF INTERESTS

The authors declare no conflict of interest.

REFERENCES CITED

De Man, B., Nuyts, J., Dupont, P., Marchal, G., Suetens, P. (1999) Metal streak artifacts in X-ray computed tomography: a simulation study. *IEEE Trans. Nucl. Sci.* 46**,** 691–696.

Ferrari, A.C. and Robertson, J. (2004) Raman spectroscopy of amorphous, nanostructured, diamond-like carbon, and nanodiamond. *Phil Trans R Soc Lond A* 362, 2477–2512.

French, B.M. (1998) *Traces of Catastrophe: A Handbook of Shock-Metamorphic Effects in Terrestrial Meteorite Impact Structures*. Houston, TX: Lunar and Planetary Institute LPI Contribution 954.

French, B.M. and Koeberl, C. (2010) The convincing identification of terrestrial meteorite impact structures: What works, what doesn't, and why. *Earth-Science Reviews* 98**,** 123–170.

Golubev, Ye.A., Shumilova, T.G. and Isaenko, S.I. (2018) Structure of natural impact glasses by microscopic data. Scanning Probe Microscopy. *IOP Conf. Series: Materials Science and Engineering* 443 (012008):1–7. https://doi:10.1088/1757-899X/443/1/012008.

Hounsfield, G.N. (1973) Computerized transverse axia scanning (tomography). Part 1: Description of system. *British Journal of Radiology* 46, 1016–1022. DOI: 10.1259/0007-1285-46-552-1016.

Isaenko, S.I., Makeev, B.A. and Shumilova, T.G. (2018) Features of studies of the structural-phase state of impact glasses of the Kara Astrobleme. *Vestnik of the Institute of Geology Komi SC UB RAS* **3**, 26–31 (In Russian).

Ivanov, M.K., Burlin, Yu.K., Kalmykov, G.A., Karnyushina, E.E., Korobova, N.I. (2008) Pertophysical methods of study of well core material (terrigenous sediments). *Textbook in two volumes. V. 1. Moscow: Moscow State University*. 112 p. (in Russian).

Maksimenko, N.I., Shumilova, T.G. and Kovalchuk, N.S. (2018) The peculiarity of the clast component of the varieties of suevites from the Kara Astrobleme. *Modern problems of theoretical, experimental and applied mineralogy (Yushkin readings-2018): Proceedings of* *the mineralogical seminar with international participation. Syktyvkar: IG Komi SC UB RAS* (In Russian).

Masaitis, V. L. (1999) Impact structures of northeastern Eurasia: The territories of Russia and adjacent countries. Meteoritics & Planetary Science, 34(5), 691-711.

Hanna, R.D. and Ketcham, R.A. (2017) X-ray computed tomography of planetary materials: A primer and review of recent studies. *Chemie der Erde - Geochemistry* 77(4), 547–572.

Hsieh, J. (2009) *Computed Tomography: Principles, Design, Artifacts, and Recent Advances*. Second ed. SPIE John Wiley & Sons Inc., Bellingham, Washington Hooken, New Jersey.

Ketcham, R.A. (2006) New algorithms for ring artifact removal. In: *Proc. SPIE 6318, Developments in X-Ray Tomography* V, San Diego, CA.

Ketcham, R.A. and Carlson, W.D. (2001) Acquisition, optimization and interpretation of X-ray computed tomographic imagery: Applications to the geosciences. *Comput Geosci* 27, 381–400.

Koeberl, C., Denison, C., Ketcham, R.A. and Reimold, W.U. (2002) High-resolution X-ray computed tomography of impactites. *Journal of geophysical research* 107(E10), 5089. doi:10.1029/2001JE001833.

Koeberl, C., Sharpton, V.L., Harrison, T.M., Sandwell, D., Murali, A.V., and Burke, K. (1990) The Kara/Ust`-Kara twin impact structure: A large-scale impact event in the late Cretaceous. In: *Global Catastrophes in Earth History* (Ed. V.L. Sharpton and P. Ward), Geological Society of America, Special Paper 247, 233–238.

Kring, D. A., Tikoo, S. M., Schmieder, M., Riller, U., Rebolledo-Vieyra, M., Simpson, S. L., et al. (2020). Probing the hydrothermal system of the Chicxulub impact crater. Science Advances, 6(22), eaaz3053.

Krumm, M., Kasperl, S. and Franz, M. (2008) Reducing non-linear artifacts of multi-material objects in industrial 3D computed tomography. *NDT & E Int* 41, 242–251.

Naumov, M. V. (2002). Impact-generated hydrothermal systems: Data from Popigai, Kara, and Puchezh-Katunki impact structures. In Plado J. & Pesonen, L. J. (Eds.) Impacts in Precambrian shields (pp. 117-171). Springer, Berlin, Heidelberg.

Naumov, M. V. (2005). Principal features of impact-generated hydrothermal circulation systems: Mineralogical and geochemical evidence. Geofluids, 5(3), 165-184.

Osinski, G.R. and Pierazzo, E. (eds.) (2013) *Impact Cratering: Processes and Products*. A John Wiley & Sons, Ltd., Publication, Blackwell Publishing Ltd. DOI:10.1002/9781118447307.

Osinski, G. R., Tornabene, L. L., Banerjee, N. R., Cockell, C. S., Flemming, R., Izawa, M. R., ... & Pontefract, A. (2013). Impact-generated hydrothermal systems on Earth and Mars. Icarus, 224(2), 347-363.

Otsu, N.A. (1979) *Threshold Selection Method from Gray-Level Histograms*. IEEE Transactions on Systems, Man, and Cybernetics SMC-9(1).

Pirajno, F. (2005). Hydrothermal processes associated with meteorite impact structures: evidence from three Australian examples and implications for economic resources. Australian Journal of Earth Sciences, 52(4-5), 587-605.

Ping-Sung Liao, Tse-Sheng Chen and Pau-Choo Chung (2001) A Fast Algorithm for Multilevel Thresholding. *Journal of Information Science and Engineering* 17, 713–727.

Rubin, A.E., Ulff-Moller, F., Wasson, J.T. and Carlson, W.D. (2001) The Portales Valley meteorite breccia: evidence for impact-induced melting and metamorphism of an ordinary chondrite. *Geochim Cosmoch Acta* 65, 323–342.

Russell, S.S. and Howard, L. (2013) The texture of a fine-grained calcium-aluminium-rich inclusion (CAI) in three dimensions and implications for early solar system condensation. *Geochim. Cosmoch. Acta* 116, 52–62.

Schmieder, M., and Kring, D. A. (2020). Earth's Impact Events Through Geologic Time: A List of Recommended Ages for Terrestrial Impact Structures and Deposits. Astrobiology, 20(1), 91-141.

Shumilova, T.G., Isaenko, S.I., Makeev, B.A., Zubov, A.A., Shanina, S.N., Tropnikov, Ye.M. and Askhabov, A.M. (2018a) Ultrahigh-pressure liquation of an impact melt. *Doklady Earth Sciences* 480(1), 595–598. DOI: 10.1134/S1028334X18050070.

Shumilova, T.G., Lutoev, V.P., Isaenko, S.I., Kovalchuk, N.S., Makeev, B.A., Lysiuk, A.Yu. and Zubov, A.A. (2018b) Spectroscopic features of ultrahigh-pressure impact glasses of the Kara astrobleme. *Scientific Reports* 8. DOI:10.1038/s41598-018-25037-z.

Shumilova, T.G., Isaenko, S.I., Ulyashev, V.V., Kazakov, V.A. and Makeev, B.A. (2018c) After-coal diamonds: an enigmatic type of impact diamonds. *European Journal of Mineralogy* 30(1), 61–76. https://doi.org/10.1127/ejm/2018/0030-2715.

Shumilova, T.G., Kovalchuk, N.S. and Makeev, B.A. (2019a) Geochemical specifics of diamond-bearing suevites of the Kara astrobleme (Pay-Khoy). *Doklady Earth Sciences* 486(1), 545–548.

Shumilova, T.G., Ulyashev, V.V., Kazakov, V.A., Isaenko, S.I., Vasil`ev, E.A., Svetov, S.A., Chazhengina, Y., Kovalchuk, N.S. (2019b) Karite – diamond fossil: a new type of natural diamond. Geoscience Frontiers. https://doi.org/10.1016/j.gsf.2019.09.011

Shumilova, T.G., Zubov, A.A., Isaenko, S.I., Karateev, I.A. and Vasiliev, A.L. (2020) Mysterious long-living ultrahigh pressure or secondary impact crisis. *Sci Rep* **10,** 2591. https://doi.org/10.1038/s41598-020-59520-3.

Shtyrlyaeva, A.A. and Zhuravlev, A.V. (2016) Increasing the resolution of X-ray microtomography. Vestnik of IG Komi Science Center UB RAS 6:24–27 (In Russian).

DOI: https://doi.org/10.2138/am-2021-7578. http://www.minsocam.org/

Shtyrlyaeva, A.A., Zhuravlev, A.V. and Gerasimova, A.I. (2016) Prospects and problems of using computer microtomography to study core samples. *Oil and gas geology. Theory and practice* 11(1) (In Russian).

Stöffler, D. and Grieve, R.A.F. (2007) Impactites. In: *Metamorphic Rocks: A Classification and Glossary of Terms, Recommendations of the International Union of Geological Sciences*/ Fettes D and Desmons J (eds.) 2.11. Cambridge: Cambridge University Press.

Tsuchiyama, A., Nakamura, T., Nakano, T. and Nakamura, N. (2002) Three-dimensional description of the Kobe meteorite by micro X-ray CT method: possibility of three-dimensional curation of meteorite samples. *Geochem J* 36, 369–390.

Uesugi, M., Uesugi, K. and Oka, M. (2010) Non-destructive observation of meteorite chips using quantitative analysis of optimized X-ray micro-computed tomography. *Earth Planet Sci Lett* 299, 359–367.

Uesugi, M., Uesugi, K., Takeuchi, A., Suzuki, Y., Hoshino, M. and Tsuchiyama, A. (2013) Three-dimensional observation of carbonaceous chondrites by synchrotron radiation X-ray CT – Quantitative analysis and developments for the future sample return missions. *Geochimica et Cosmochimica Acta* 116, 17–32.

Wellington, S.L. and Vinegar, H.J. (1987) X-ray computerized tomography. *Journal of Petroleum Technology* 39, 885–898.

TABLE CAPTIONS

TABLE 1. Description of the studied samples of impactite varieties from the Kara astrobleme.

TABLE 2. Porosity data in different types of impactites of the Kara astrobleme.

FIGURE CAPTIONS

FIGURE 1. X-ray tomographic artefacts in the specimen of impactite from the Kara astrobleme: a – apparent increase in X-ray attenuation coefficients in the peripheral part of the sample (red indicates artefacts and pore space), specimen overview. b - X-ray tomographic artefacts on a sample slice.

FIGURE 2. Examples of artefacts formed as a result of the specifics of imaging (S2) and setting standards on the specimen (S3, S4) (S1 is the area with minimal influence by the artefacts), axial section of the specimen. The standards are labelled Gr (graphite), Q (quartz), and Ca (calcite), while the sample of clast-poor melt rock is located at the bottom of the image with artifacts zones S1, S2 and S3. The sample diameter – 4 cm.

FIGURE 3. The measured attenuation coefficients for the used mineral standards: air (purple), graphite (red), quartz (green), calcite (yellow).

FIGURE 4. Plots of the dependence of attenuation coefficients on X-ray energy for the standards, designed by MuCalcTool (Hanna and Ketcham, 2017).

FIGURE 5. Comparison of natural slices of suevites and melt impactites (A-E) with the corresponding tomographic sections (F-J).

FIGURE 6. Multimodal histograms of the frequency distributions of the attenuation coefficients of the matrix (M(1-3)), fragments of target rocks (C(1-4)) and strongly porous altered aluminosilicate melt fragment (L1) on an X-ray tomographic section: a – suevite Kr-135; b – matrix; c – fragment; d – total histogram. The specimen diameter – 4 cm.

FIGURE 7. Suevites X-Ray tomograms: reconstruction of the distribution of CT data values (a-c), morphology of pore space and/or carbon substance (d-f), carbonate component (g-i) and sulfides (j-l) of three types of suevites (Kr-232, Kr-61, and Kr-135). The scale is the same in all images.

FIGURE 8. Clast-poor melt rock X-ray tomogram (Kr-72): a – initial clast-poor melt rock tomogram; b – pore space and/or carbon substance of melt rock; c – spatial relationships of melt rock matrix (grey), pore space and/or carbon substance (red) and carbonate component (blue).

FIGURE 9. X-ray tomogram of melt inclusions in suevite II and reconstruction (Kr-41): a – tomogram image of fluid texture in the impact melt clast; b – reconstruction of two contrasting phases (blue – dense anatase-orthoclase, green – less dense anatase-orthoclase with carbon particles); c – reconstruction of pore space and/or carbon substance.

FIGURE 10. Raman spectra of the studied clast melt rock sample and reference standard spectra: a–c – anatase-orthoclase aggregate (a – component 1, dense; b – component 2, less dense; c – reference spectrum of orthoclase); d – reference spectrum of anatase; e – spectrum of carbon particle from component 2; f – standard spectrum of glass-like carbon.

FIGURE 11. SEM image and electron microprobe elemental mapping of the melt fragment Kr-41: a – secondary electron image; b – corresponding multi-element map; Si, Al, O, Ca, K and C - maps for individual elements. CM – crystallized impact melt, GL – impact glass, CR – carbon-rich field, CP – carbon-poor field.

Table 1. Description of the studied samples of impactite varieties from the Kara astrobleme

Variety of impactite	Sample number	Sampling region	General characteristics	Texture	Prevalent color	Prevalent substrate
Impact melt rock	Kr-232	River Anaroga	Silica-rich	Massive	Brownish	Polymictic sandstone
Impact melt clast	Kr-41	River Kara	Silica-rich	Fibrous	Light-yellow/ grey	Polymictic sandstone
I type suevite	Kr-61	River Kara	Carbonate-rich	Clastic	Light brownish	Polymictic sandstone
II type suevite	Kr-72	River Anaroga	Silica-rich	Clastic	Grey	Limestone
III type suevite	Kr-135	River Sopchau	Carbon-reach	Clastic	Dark grey to black	Black shales, coals

Table 2. Porosity data in different types of impactites of the Kara astrobleme

Studied parameters	Suevite (clastic impactite)						Melt rock	Melt clast in suevite
	Kr-135		Kr-232		Kr-61		Kr-72	Kr-41
	Total	Matrix	Total	Matrix	Total	Matrix	Total	Total
Studied volume[a], million voxels	1215	15	1136	15	1427	15	1231	1167
Porosity[a], %	3.99	0.08	0.22	0.17	0.31	0.18	0.37	0.26
Porosity (open)[b], %	14	-	no	-	7	-	-	-

Notes: a. X-Ray microtomography; b. I.A. Preobrazhensky`s method; total – total porosity; matrix – porosity of matrix.

Figure 1

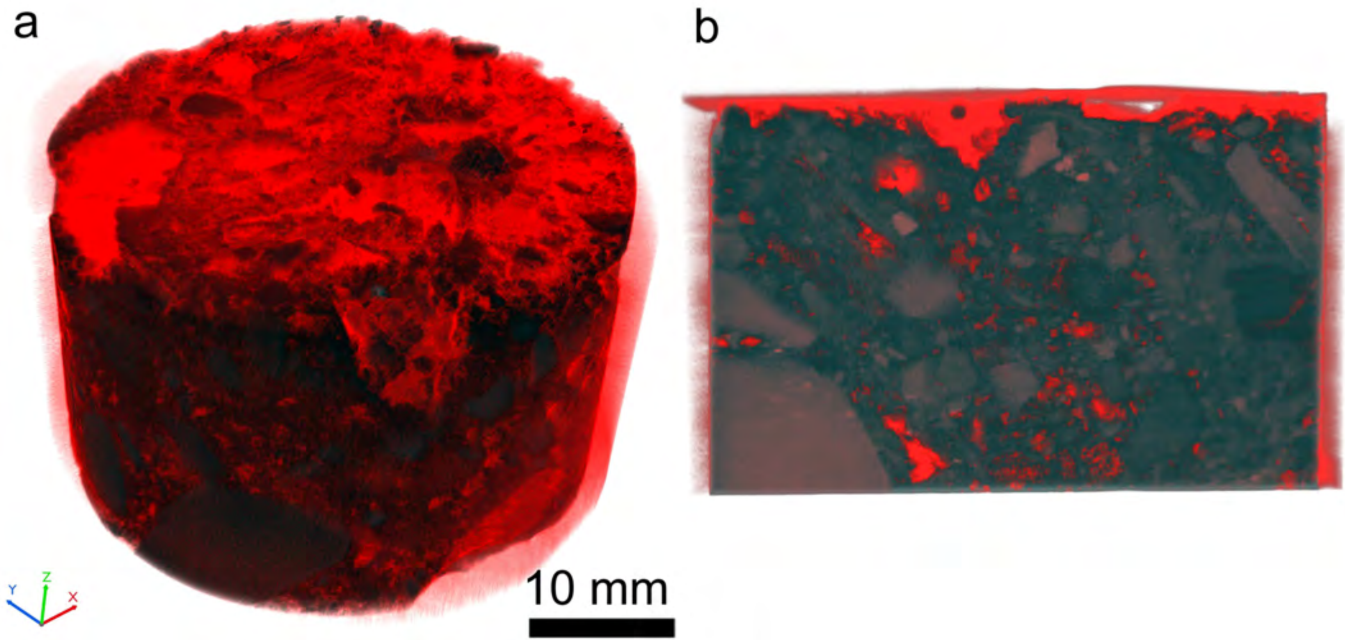

Figure 2

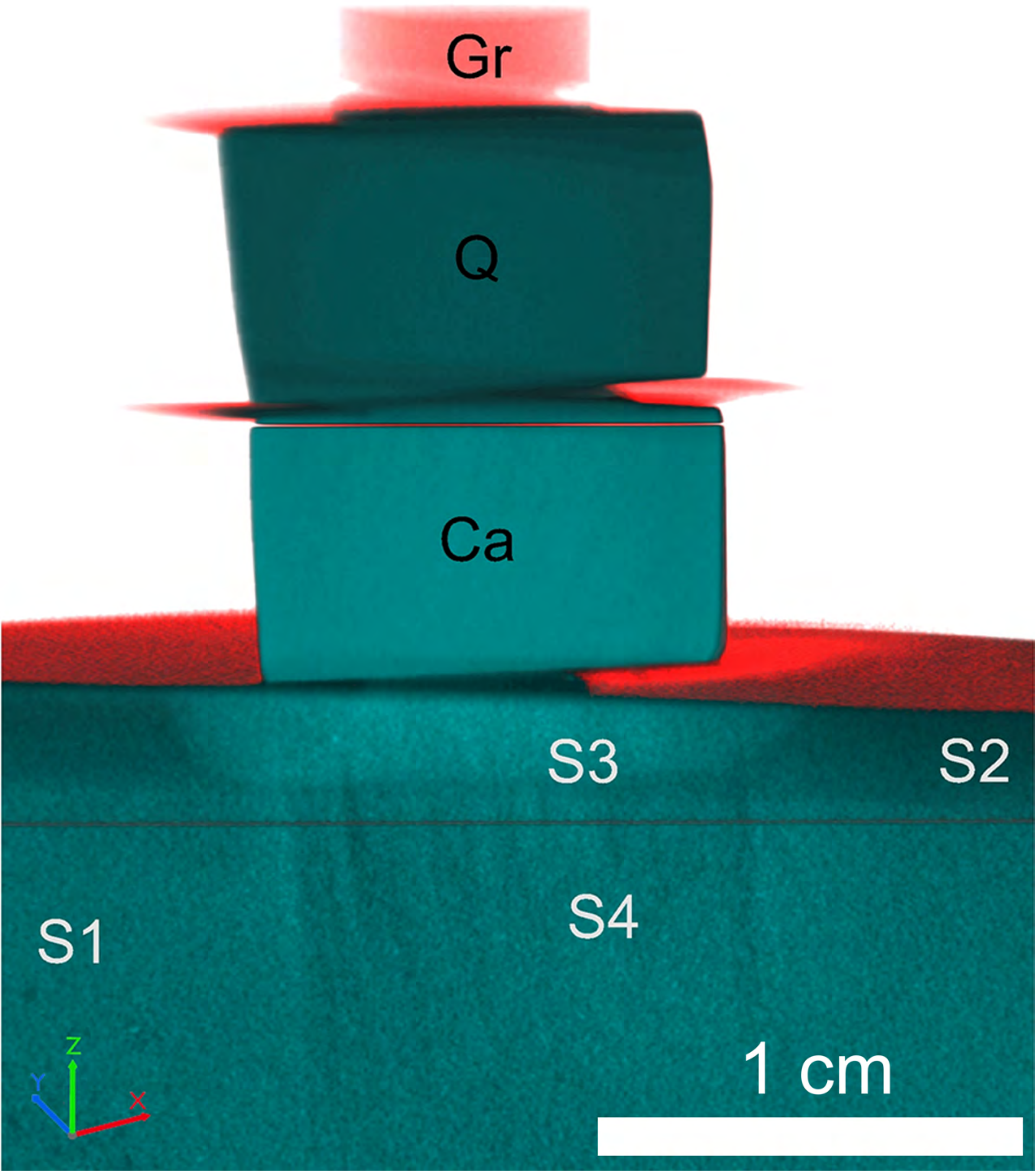

Figure 3

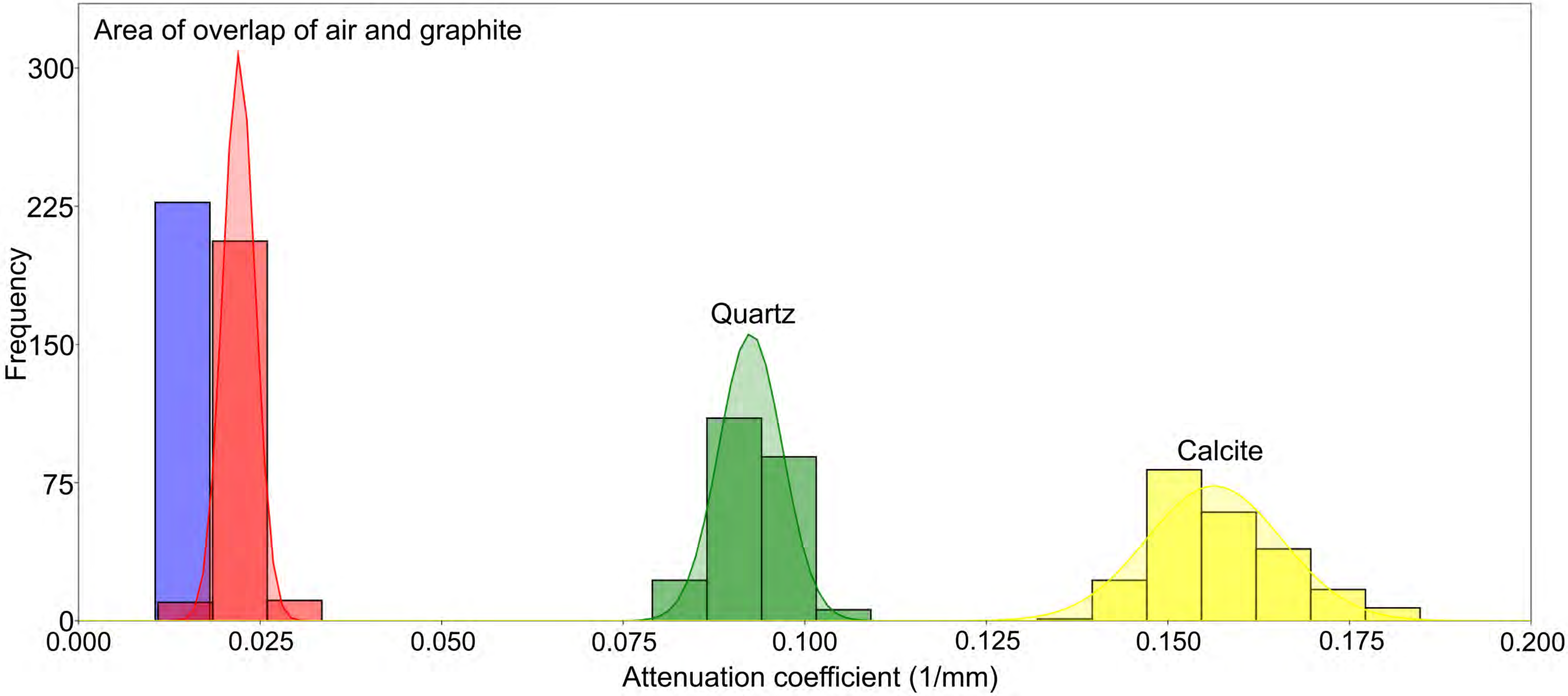
Area of overlap of air and graphite
Quartz
Calcite
Frequency
300
225
150
75
0
0.000
0.025
0.050
0.075
0.100
0.125
0.150
0.175
0.200
Attenuation coefficient (1/mm)

Figure 4

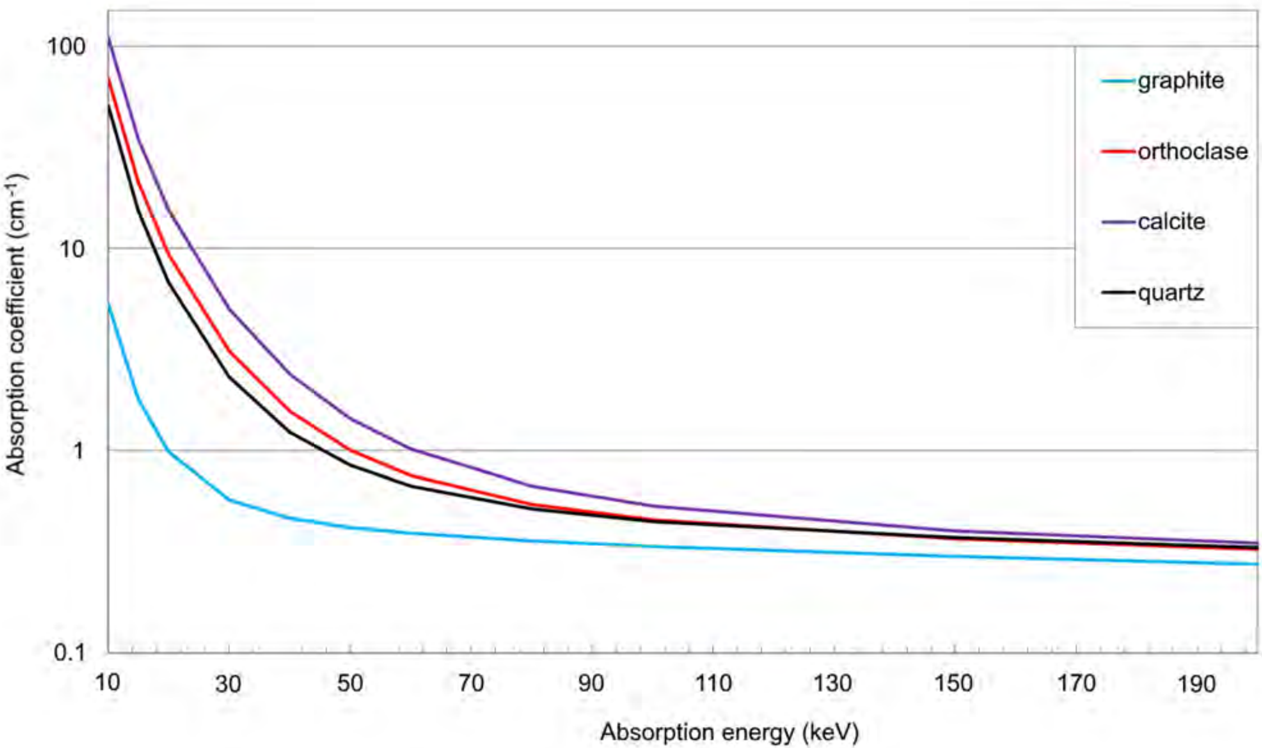

graphite
orthoclase
calcite
quartz
Absorption coefficient (cm-1)
100
10
1
0.1
10
30
50
70
90
110
130
150
170
190
Absorption energy (keV)

Figure 5

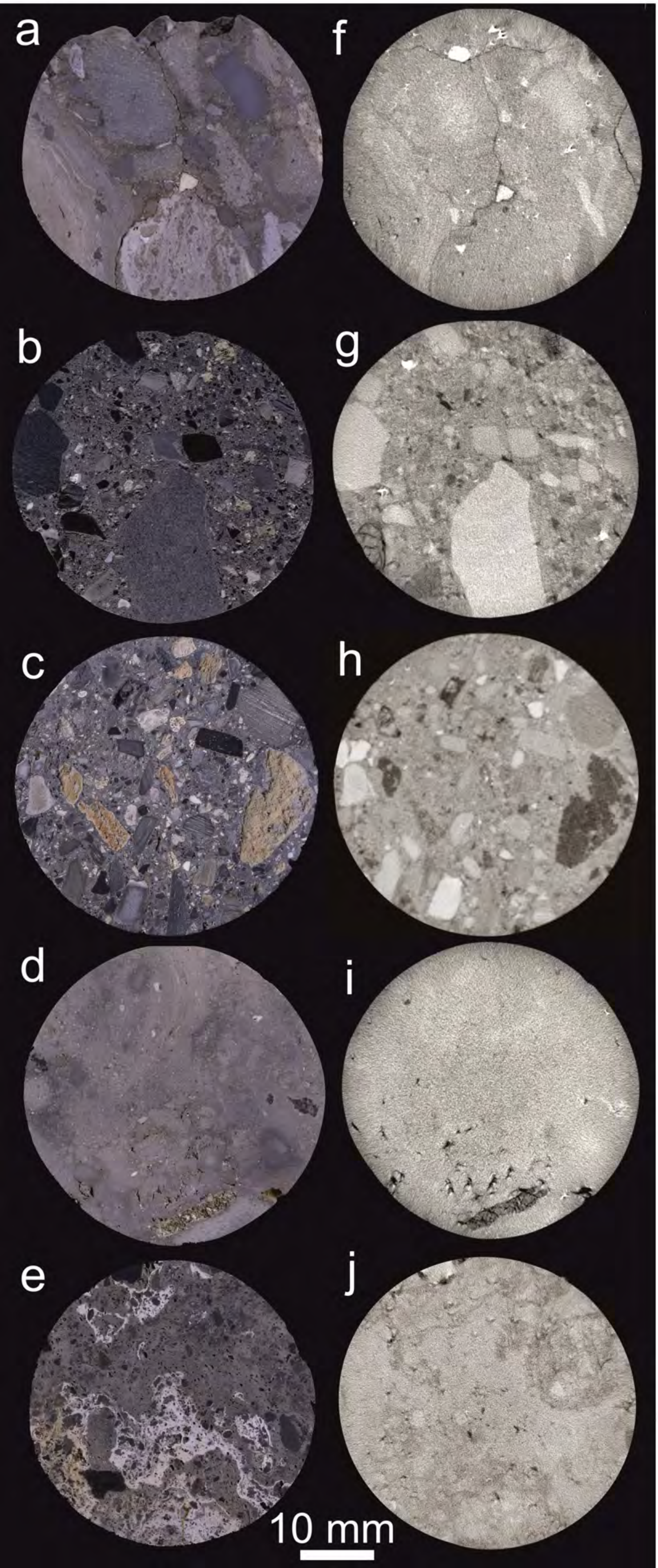

Suevite (type I)
Sample Kr-232

Suevite (type II)
Sample Kr-61

Suevite (type III)
Sample Kr-135

Clast-poor
melt rock
Sample Kr-72

Melt inclusion
Sample Kr-41

Figure 6

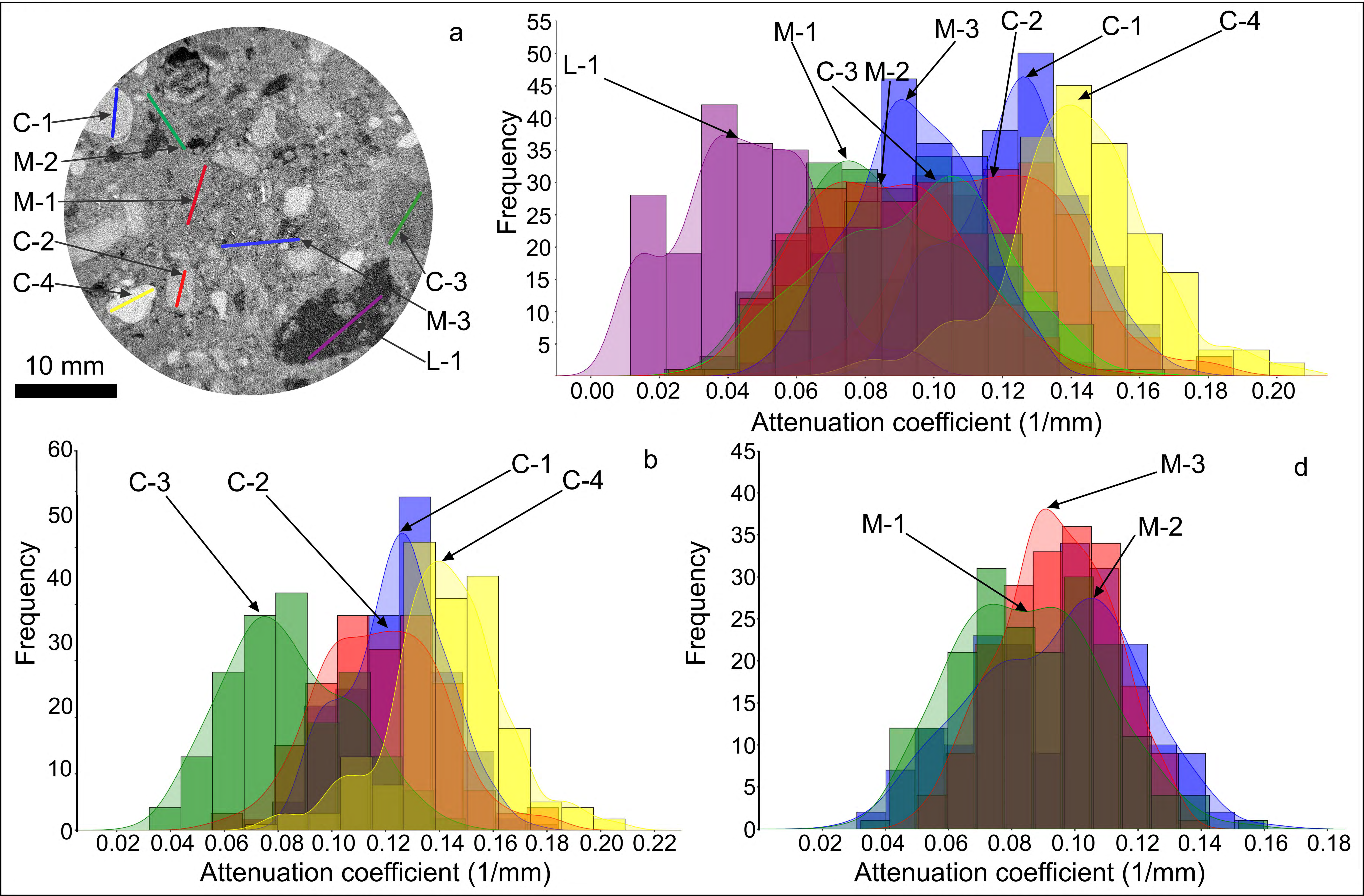
a
C-1
M-2
M-1
C-2
C-4
C-3
M-3
L-1
10 mm
Frequency
Attenuation coefficient (1/mm)
b
C-3
C-2
C-1
C-4
d
M-3
M-1
M-2

Figure 7

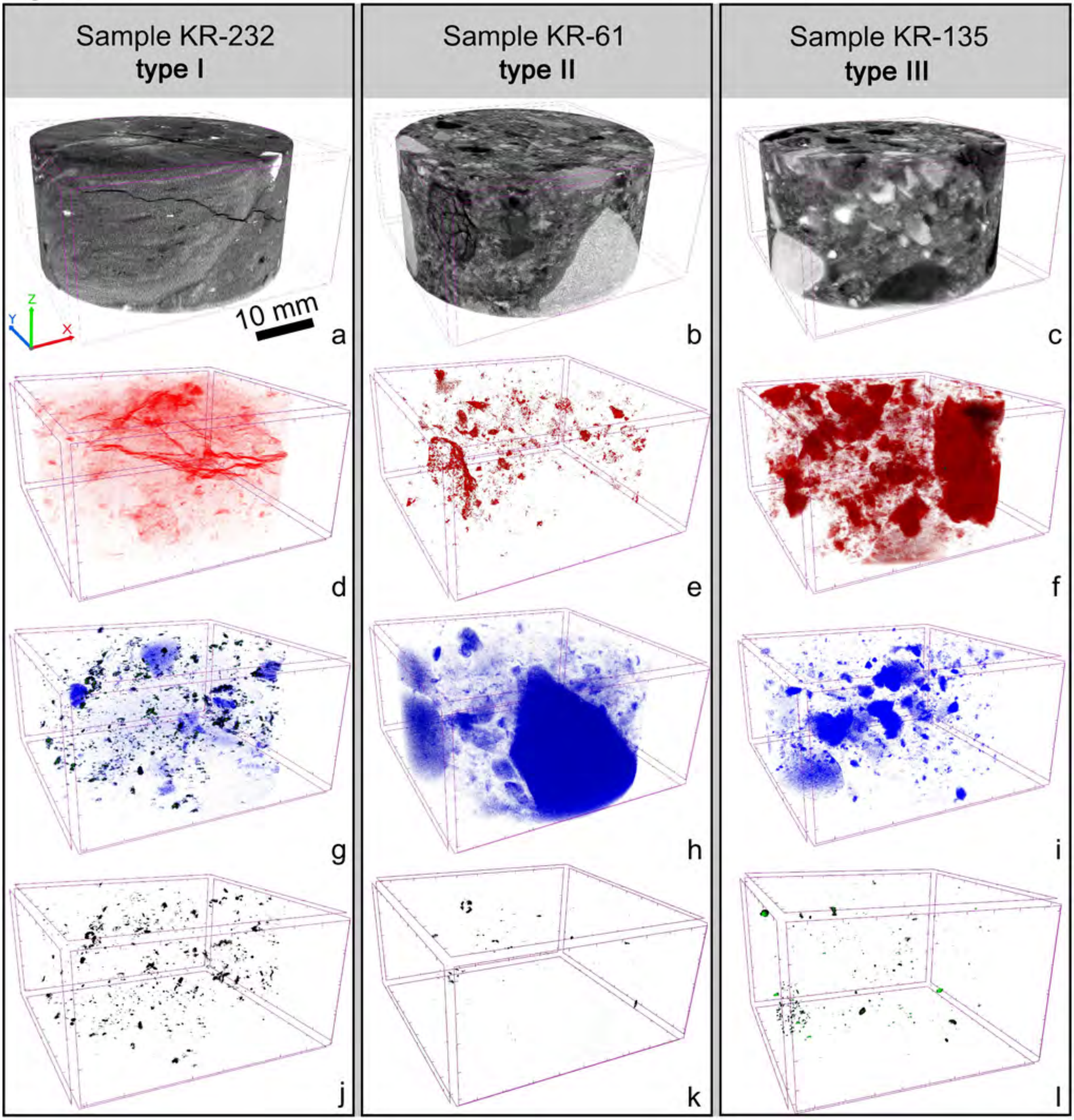
Sample KR-232
type I
Sample KR-61
type II
Sample KR-135
type III
Z
Y
X
10 mm
a
b
c
d
e
f
g
h
i
j
k
l

Figure 8

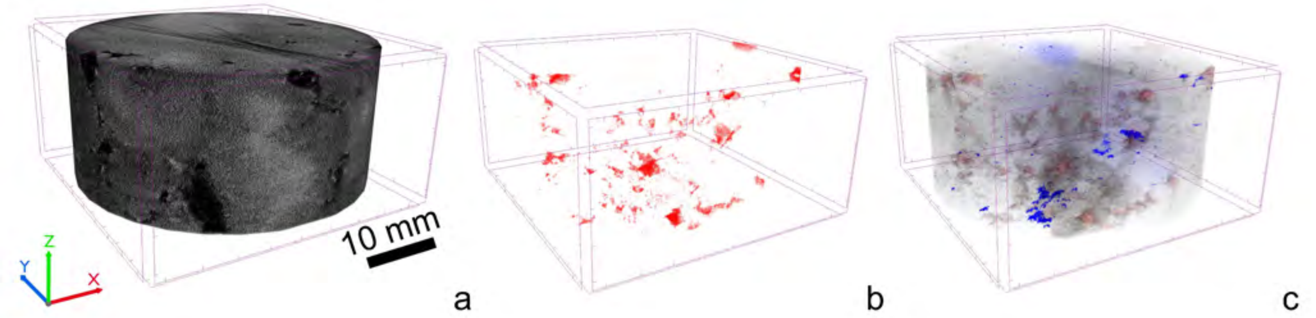

Figure 9

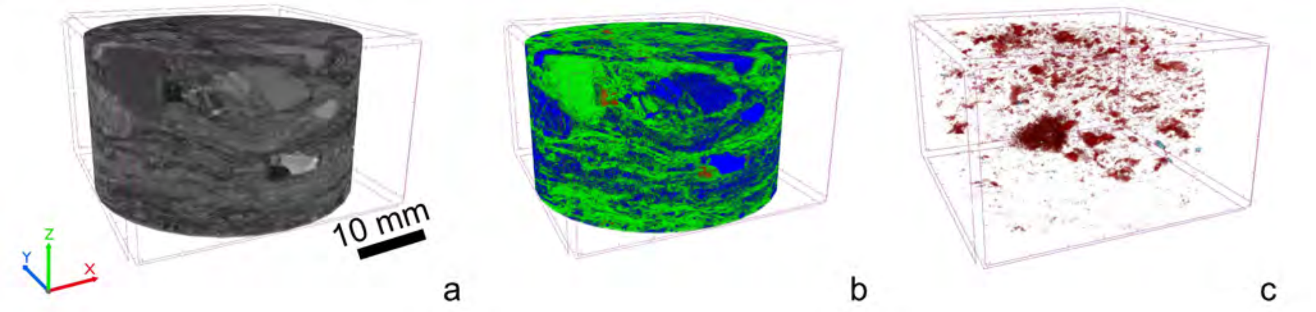

Figure 10

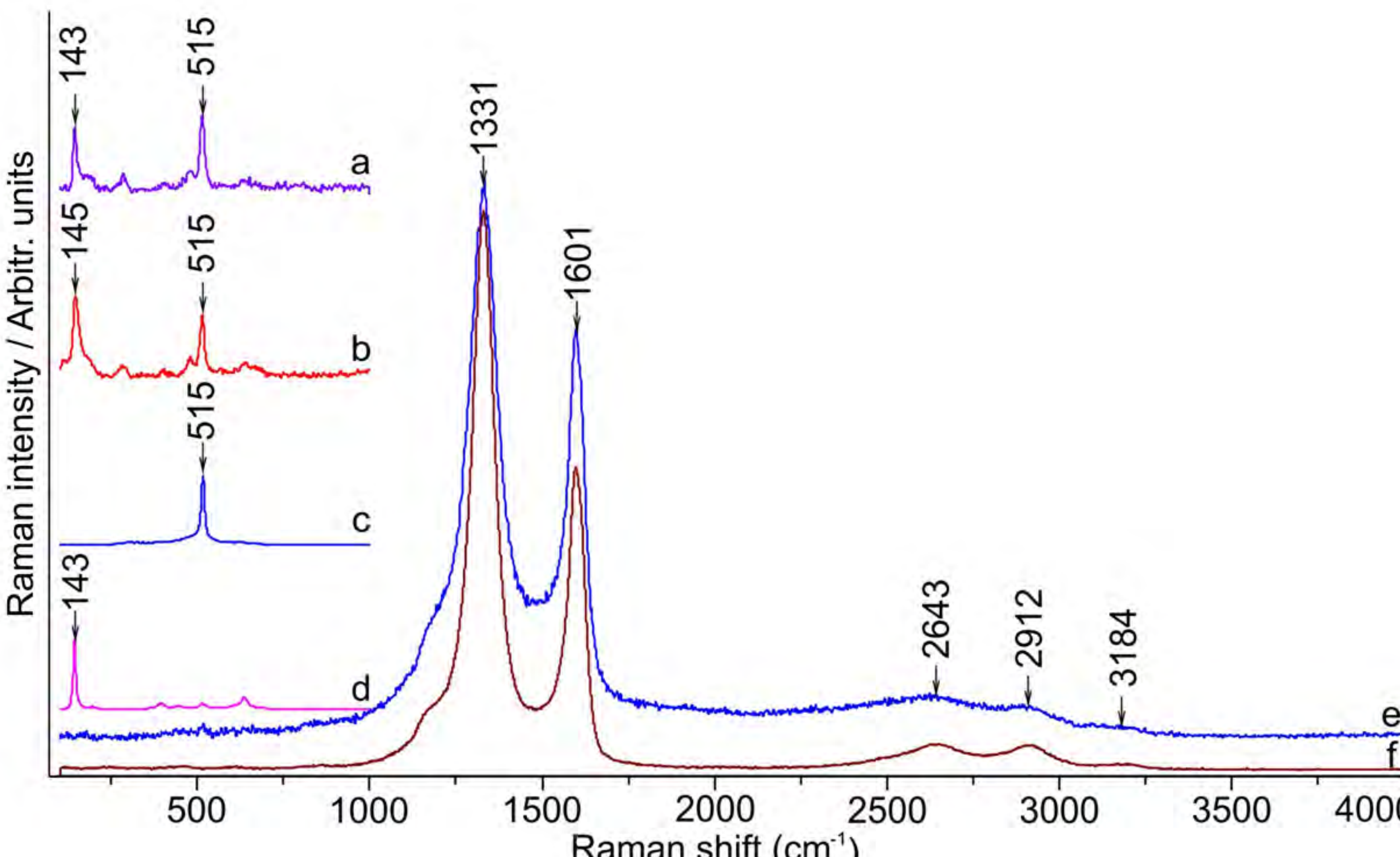
143
515
a
145
515
b
515
c
143
d
1331
1601
2643
2912
3184
e
f
Raman intensity / Arbitr. units
500
1000
1500
2000
2500
3000
3500
4000
Raman shift (cm-1)

Figure 11